JOURNAL OF APPLIED PHYSICS **114**, 143901 (2013)

# Spin valve effect across the metal-insulator transition in $V_2O_3$

Mikhail Erekhinsky, J. de la Venta, and Ivan K. Schuller
*Department of Physics and Center for Advanced Nanoscience, University of California San Diego, La Jolla, California 92093, USA*

(Received 31 July 2013; accepted 19 September 2013; published online 7 October 2013)

The magnetoresistance of Ni/$V_2O_3$/Py devices shows interesting behavior in the temperature dependence across the $V_2O_3$ metal-insulator transition. A spin-valve effect (~0.1%) is found below the transition temperature when $V_2O_3$ is in the insulating phase. Contrary to expectation, the spin-valve effect disappears when device is heated above 150 K and $V_2O_3$ is in the metallic state. At these temperatures, the behavior of the device is governed by anisotropic magnetoresistance of Ni. Using finite method analysis of our device we show that disappearance of the spin-valve effect cannot be explained by changes in the current distribution with temperature. © *2013 AIP Publishing LLC*. [http://dx.doi.org/10.1063/1.4824294]

## I. INTRODUCTION

The implementation of spintronics[1,2] in transition metal oxides requires a physical understanding of the creation, detection, and manipulation of a spin current in these materials. Transition metal oxides are systems inherently sensitive to weak external stimuli and are known to radically change their physical properties under weak perturbations.[3,4] These oxides then open up the possibility of studying a variety of magnetic phenomena all the way from spin transport to exchange bias.[5,6] Implementing spintronic devices based in transition metal oxides is challenging because of the resistivity mismatch[7] between oxides and common ferromagnetic (FM) materials, such as Ni, Co, and Fe, which prevents efficient spin injection.[7–9] A common approach to solve this problem is to control the FM/semiconductor (SC) interface by decreasing its conductivity.[10,11] This can be achieved by including a tunnel barrier between the ferromagnet and the semiconductor. An interesting possibility arises from studying spin injection when the resistivity mismatch between the FM and the oxide changes orders of magnitude due to the oxide metal to insulator transition (MIT). The MITs are of first order and are accompanied by distinct structural transformations.[12–14] Vanadium oxides are of special interest since they give rise to a series of compounds with closely related crystal structures which undergo a MIT. These different phases of vanadium oxides then open up the possibility of studying the effect of conductivity changes on spin transport and spin propagation across the MIT.

The purpose of this study is to investigate the possibility of spin injection and propagation through $V_2O_3$ with transparent interfaces. This oxide has a first order MIT, accompanied by crystal structure changes at 160 K.[12,13,15] Above 160 K, $V_2O_3$ is a paramagnetic metal and below it is an anti-ferromagnetic (AFM) insulator (semiconductor). Thus, it is a suitable system that allows studying the effect of the material resistance change on the spin transport.

We studied temperature evolution of magnetoresistance of more than 50 Ni/$V_2O_3$/Py sandwich devices with current perpendicular to the plane (CPP).[16] Anisotropic magnetoresistance (AMR) of Ni and Py layers was measured independently on the same sample to confirm different reversal fields for all temperatures. Evolution of the magnetoresistance of the devices with temperature between 20 K and 300 K at 10 K intervals was measured. Above the transition temperature, the magnetoresistance of the device is dominated by AMR of Ni. Contrary to expectation from the resistivity mismatch, only at temperatures below the MIT, the device magnetoresistance exhibits a spin-valve (SV) effect. This is confirmed in similar samples but replacing the Py top layer with Ni or non-magnetic Nb.

We performed extensive finite element calculations to simulate the current distributions in the device. It was found that the current flows mostly straight between the top and the bottom contacts. At 20 K, it is evenly distributed over the $V_2O_3$ layer at the intersection of the top and the bottom contacts, although at 300 K the current distribution is very inhomogeneous. Nevertheless, the contributions of the different layers to the total measured resistance were estimated for different temperatures. The results show that at the temperatures below MIT most of the measured resistance originates from the current flow though the $V_2O_3$ layer. At higher temperatures, the $V_2O_3$ contribution decreases but still accounts for at least half of the measured resistance. Additional analysis suggests that the disappearance of SV effect at high temperature cannot be simply attributed to a change in the current distribution in the $V_2O_3$ layer.

## II. EXPERIMENTAL

### A. Fabrication

A series of devices with CPP geometry were prepared. Figure 1(a) shows a vertical cross section of a device. Instead of a standard cross geometry (straight top and bottom contacts cross in perpendicular directions),[17] an intersection of two 90° corners was used, see Figure 1(b).

The fabrication process starts with standard photolithography and lift-off to define the bottom contact, common for all devices. The different layers were deposited by RF sputtering, the details of which can be found elsewhere.[15] For bottom contact and as the first FM material, 40 nm of Ni was deposited at room temperature with a 5 nm capping layer of $V_2O_3$ to prevent oxidation and contamination of the Ni/$V_2O_3$ interface. After lift-off, the sample was loaded back into the

 

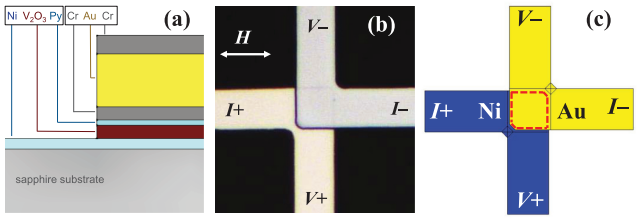


FIG. 1. (a) Schematic drawing of a Ni/$V_2O_3$/Py device, side view, showing different layers; and (b) microscope image of a device, view from the top. Direction of applied magnetic field, $H$, as well as electrodes used for applying current and measuring voltage are indicated. (c) Geometry of the simulated device. Red dashed contour indicates the location of the $V_2O_3$ layer at the intersection of the Ni (blue) and Au (yellow) contacts.

sputtering chamber for deposition of 13 to 65 nm of $V_2O_3$ at 750 °C. After cooling to room temperature, 15 nm of permalloy (Py, $Ni_{80}Fe_{20}$) was deposited as the second FM layer without breaking the vacuum.

The second photolithography was done to define the top Cr/Au/Cr contacts in a specific position to match the corners of the bottom Ni contact. The thickness of the gold was 250 nm, and the thicknesses of two Cr layers were 50 nm on the bottom for adhesion and 70 nm on the top to act as a solid mask during plasma etching.

Finally, the whole sample was dry etched in two steps: first, with high power argon plasma to break through the top Py/Cu layer, and second, with $Cl_2$ plasma to quickly etch vanadium oxide. Since $Cl_2$ does not form volatile compounds with Ni, the bottom contact remained intact after etching. Cr/Au/Cr contacts preserve the $V_2O_3$/Py layers under them. As a result, $V_2O_3$/Py remains only under the top contact, including the intersection of the bottom and the top contacts, which forms a Ni/$V_2O_3$/Py sandwich structure with approximately $10 \times 10\ \mu m^2$ area, Figure 1(b).

### B. Characterization

X-ray diffraction was performed on the whole Ni/$V_2O_3$/Py trilayer, deposited on a separate substrate simultaneously. The Ni and Py grow in the (111) direction, and $V_2O_3$ grows on top of Ni in (001) direction, for diffraction patterns, see Figure 2 in Ref. 15.

Electrical transport measurements of CPP devices were done in a liquid helium flow cryostat as a function of temperature and magnetic field. Typically, the samples were cooled in zero field to 20 K.[18] Later the temperature was stabilized at 10 K intervals up to 300 K. At each of those temperatures, the magnetoresistance of a device was measured using a dc current source and a nano-voltmeter. The contacts schematics used for current and voltage are shown in Figure 1(b), as well as the direction of applied in-plane magnetic field. The field was swept between positive and negative value of $H_{max} = 1.2$ kOe, well above the saturation fields of Ni or Py layers.

## III. RESULTS AND DISCUSSION

### A. $V_2O_3$ transition

To investigate the spin transport in the metallic and insulator (semiconductor) phases of $V_2O_3$, it is important to assure that the $V_2O_3$ grown under these conditions shows a MIT. In thin films, the magnitude and temperature of the MIT depends on the substrate, deposition parameters, and film thickness.[19–23] When $V_2O_3$ is grown on Ni, it is difficult to measure the transition since the usual in plane resistance is dominated by the low resistivity of metallic Ni film. The CPP geometry with all the current through the $V_2O_3$ layer allows a more accurate measurement of $V_2O_3$ transition, as it will be shown in Sec. IV, where we simulated the current and voltage distribution through the device.

Therefore, first we measured the resistance of the devices as a function of temperature at 1.2 kOe magnetic field, when the magnetizations of both FM layers are saturated. Figure 2 shows three examples of $R_{sat}(T) = R(H_{max}, T)$ for devices with different $V_2O_3$ thicknesses: 65 nm (black solid squares), 39 nm (green empty circles), and 26 nm (orange solid triangles). For the thickest device, the resistance changes from ~3 Ω at 20 K to ~0.2 Ω at 300 K, an order of magnitude MIT at approximately 160 K. However, for thinner devices, the size of the transition diminishes, and the metallic behavior appears below the transition temperature, Figure 2. This shows that the resistance of the whole device is very sensitive to $V_2O_3$ thickness. One possible explanation is that the magnitude of the resistance change across the MIT of $V_2O_3$ layer decreases with smaller thickness,[23] another is that roughness and pinholes in the $V_2O_3$ layer might reduce the measured resistance.[24] In addition, misalignment between top and bottom contacts during the fabrication process cannot be discarded: based on measured Ni resistivity in our devices, 1 $\mu$m misalignment could add up to 0.3 Ω to the total device resistance. For thinner devices, the resistance of $V_2O_3$ layer is smaller, resulting in a larger relative contribution of the in-plane resistance of metallic contacts; thus, explaining the metallic behavior at low $T$ in these devices. The exact magnitude of the transition of $V_2O_3$ layer is hard to establish for each thickness. Nevertheless, for all thicknesses of $V_2O_3$, including the 13 nm sample, there is a clear signature of MIT in the temperature dependence of the resistance, Figure 2. The resistivity values of $V_2O_3$ and the

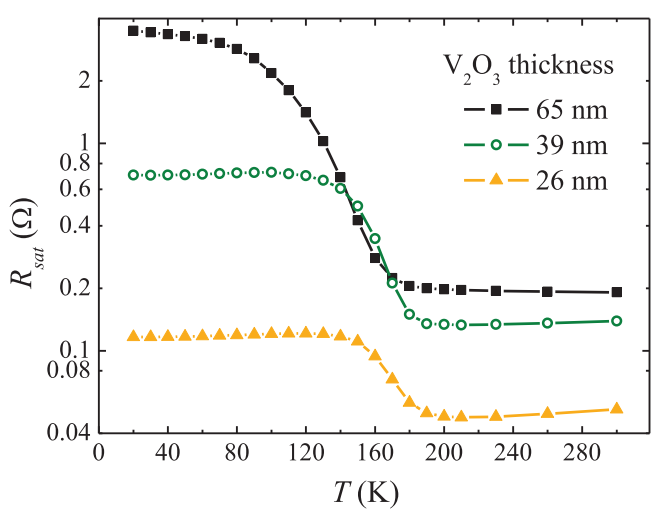


FIG. 2. $R$ vs. $T$ of the devices with 3 different $V_2O_3$ thicknesses: 65 nm (black solid squares), 39 nm (green empty circles), and 26 nm (orange solid triangles), showing the changes of the MITs with thickness.

effect of the misalignment between contacts are discussed in Sec. IV.

### B. Magnetoresistance

There are two possible effects that may be expected in the MR of these devices: AMR[25,26] and SV effect.[27–32] In the first, the resistance of a FM layer depends on the angle between the electrical current and local magnetization.[25,28] The maximum (minimum) of the resistance is measured when the current is parallel (perpendicular) to the magnetization. Thus, measuring AMR in a ferromagnet is also a convenient way to identify coercivities in mesoscopic ferromagnetic structures.[33] When the current is applied perpendicular (parallel) to the magnetic field, the maxima (minima) in the magnetoresistance indicate the fields at which the magnetization reverts, i.e., the reversal fields.

In the SV effect, the resistance of the FM1/NM/FM2 sandwich depends on the relative orientation of magnetizations of the two FM layers.[28,32] The lowest resistance is measured in the parallel (P) state when both magnetizations are pointing in the same direction, and the highest corresponds to the anti-parallel (AP) state when the magnetizations are pointing in opposite directions. Therefore, if the two ferromagnets in the device have different reversal fields, then by sweeping the magnetic field it is possible to measure the change from low in the P state to high resistance in the AP state.

Thus, before investigating the magnetoresistance of the Ni/$V_2O_3$/Py device, it is important to determine the fields at which Ni and Py layers reverse their magnetizations, i.e., their coercivities, $H_C$. For that purpose, in each sample, the Ni AMR was measured in the straight section of bottom contact between two adjacent devices, which was chosen to be perpendicular to the magnetic field. An example AMR measured at $T = 20$ K is shown in the inset of Figure 3. The Py AMR could only be measured in combination with other materials comprising the top contact, $V_2O_3$/Py/Cr/Au/Cr; nevertheless, the relevant peaks in the MR curves were clearly visible.

Figure 3 shows the reversal fields for both Ni and Py layers. For all temperatures, Ni has higher reversal fields than Py. Therefore, for the magnetic fields above $H_C$ of Py and below $H_C$ of Ni, the magnetizations of the two FM layers point in opposite directions. For the fields smaller than $H_C$ of Py or larger than $H_C$ of Ni, the magnetization directions are the same.

The magnetoresistance change is defined as $\Delta R = R - R_{sat}$, where $R_{sat}$ is the resistance measured at the maximum applied magnetic field $H_{max}$. For all measured temperatures, $\Delta R$ was small in comparison with changes of $R_{sat}$ with $T$. The normalized MR, $\Delta R/R_{sat}$, reaches its maximum of 2%–3% at temperatures above the MIT. At the same time, $\Delta R/R_{sat}$ is only 0.1%–0.2% at low $T$, due to either high values of $R_{sat}$ or low values of $\Delta R$. Therefore, to understand how the features of MR evolve with increasing temperature, a color map of $\Delta R$ (instead of $R$ or $\Delta R/R_{sat}$) was plotted in Figure 4(a) as a function of magnetic field (horizontal axis) and temperature (vertical axis). Five slices of this plot, indicated by the black horizontal lines and corresponding to $T = 30$, 80, 130, 180, and 260 K, are shown in Figure 4(b). It is important to note that both Figures 4(a) and 4(b) shows only positive field sweep direction ($-H_{max} \rightarrow +H_{max}$). The opposite field sweep is symmetric around zero field.

At high $T$ (>130 K), there is a peak at H ~ 100 Oe on top of a smooth background, Figure 4(b). The background increases with magnetic field magnitude. On the other hand, at low temperature, there is a plateau between approximately 0 and 200 Oe. In this case, the gradual background decreases with applied field magnitude. The evolution of the

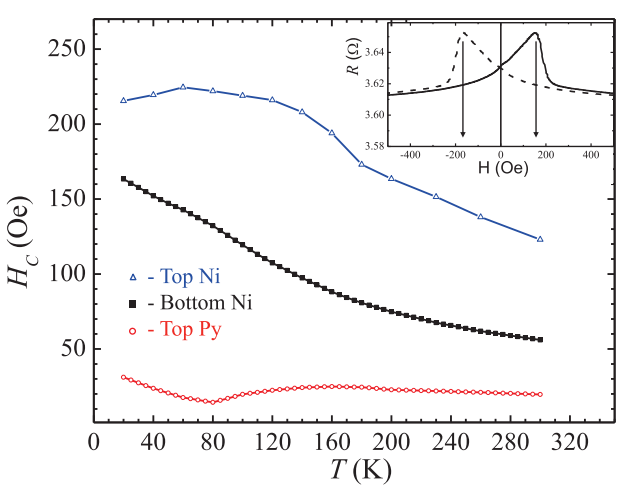


FIG. 3. Coercivities, $H_C$, of bottom Ni layer (black solid squares), top Py layer (empty red circles), and top Ni layer for Ni/$V_2O_3$/Ni sample (blue empty triangles). Inset: example AMR of the bottom Ni contact at 20 K. Solid and dashed lines show positive and negative magnetic field sweeps, respectively. The coercivities are given at the peaks positions, indicated by the arrows.

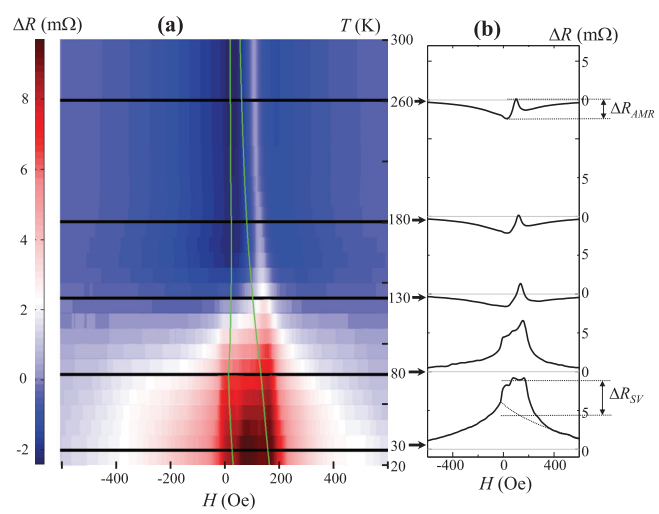


FIG. 4. (a) Temperature evolution of $\Delta R(H)$ for Ni(40)/$V_2O_3$(65)/Py(15) device (positive field sweep only). Two light-green (light-grey) vertical curves indicate the reversal fields of FM layers (also shown on Figure 3). (b) 5 examples of $\Delta R(H)$ for 5 different $T$ (positive field sweep only—indicated by black arrows), corresponding to the black horizontal lines on (a). Each curve is offset by 0.01 Ω. The magnitude of the SV effect, $\Delta R_{SV}$, is taken as the resistance difference between the plateau height and the extrapolation of the smooth background, demonstrated by the dashed lines on the 30 K slice. The magnitude of AMR effect, $\Delta R_{AMR}$, is taken as a peak to peak position, demonstrated by the dashed lines on the 260 K slice.

magnetoresistance features with temperature can be seen in Figure 4(a): when the temperature of the device increases, the low $T$ plateau gradually disappears and the high $T$ peak appears.

The reversal fields of FM layers are also added to the color map plot, two light-green (light-grey) vertical curves in Figure 4(a), to correlate them with the magnetoresistance of the Ni/$V_2O_3$/Py device. Interestingly, the peak in the magnetoresistance of the device above 130 K occurs at fields higher than $H_C$ of both Py and Ni. Similar magnetoresistance was reported earlier in a Ni film with the magnetic field applied at angles near 45° from the current direction.[34] In Ref. 34, the positions of the peaks is also at slightly higher fields than the minima (maxima) observed for AMR measured for 0° (90°) between the field and current direction, similar to observed in Figure 4. This suggests that the high T magnetoresistance of the device is due to the bottom Ni layer AMR with non-collinear applied current.

The plateau at low $T$ starts at fields slightly smaller than the $H_C$ of Py and ends at fields slightly higher than the $H_C$ of Ni (for positive field sweep direction). The plateau can be attributed to either the SV effect (because the observed increase in resistance is approximately at fields between the $H_C$ of Py and $H_C$ of Ni) or to the sum of two AMR signals, one from Ni and another from Py, Figure 4(b).

### C. Additional samples

To differentiate between the two possible situations at low temperatures and to confirm the proposed explanation at high temperature, two additional samples were made, with 6 devices on each sample. The top Py layer was substituted with non-magnetic Nb in one sample, and with Ni in another. In the latter case, the bottom and the top Ni layers have different $H_C$ due to the difference in thicknesses: 40 nm vs. 15 nm. The dependence of the coercivity of the top Ni layer on temperature is also plotted in Figure 3.

Figure 5 shows the normalized magnetoresistances of the three samples at 20 and 300 K. At 20 K, Figure 5(a), the device with top Py layer shows a plateau between 0 Oe and 200 Oe, similar to a different device shown in Figure 4. The device with the top Ni layer also has a plateau, but shifted to higher fields, between 200 Oe and 400 Oe. Interestingly, the device with Nb does not have a plateau at any field. These unambiguously rules out the sum of two AMR signals as the explanation of the MR at low T in favor of the spin-valve effect. The shift of the plateau in Ni/$V_2O_3$/Ni device to higher fields is consistent with this explanation and is due to a larger coercivity of the top Ni layer. For positive field sweep, in this case, bottom layer switches first, causing the antiparallel configuration of the two FM layers, and at a higher field the top Ni switches as well, restoring the parallel configuration.

At 300 K, all three samples, including the sample with Nb, exhibit very similar behavior, Figure 5(b). Moreover, the position of the peak in MR is approximately the same for all three samples. This confirms earlier suggestion that at high temperature the behavior of the device is dominated only by the AMR of the bottom Ni layer.

### D. Thickness dependence of MR

Besides the difference in the MR shape at low and high $T$, the size of the effect also changes. For all devices, the size of the low temperatures spin-valve effect (resistance difference between the smooth background and the plateau height, see Figures 4(b) and 5(a)) does not exceed 0.2%. On the other hand, the high temperature AMR amplitude (resistance difference between the minimum and maximum points of the curve, Figure 4(b)) varies between 1% and 2% for different samples. To check whether this is a consequence of the normalization to the total resistance which changes by a factor of 10 from low to high $T$ for 65 nm of $V_2O_3$, a series of samples with different $V_2O_3$ thicknesses were studied. These results averaged over few devices for each $V_2O_3$ thickness are plotted in Figure 6. The number of devices is different for all thicknesses. For example, magnetoresistance of 5 devices with 26 nm and more than 20 devices with 65 nm were measured. The error bars indicate standard deviations from average value for devices with specific thickness. The variation arises from significant differences in both $R_{sat}$ and $\Delta R$ even for devices on the same sample. As mentioned above, this likely due to the imperfect matching and randomly distributed pinholes that create small shorts between the bottom and top contacts. Figure 6 shows that the SV effect at 20 K is one order of magnitude smaller than the AMR at 300 K. This is true even for thinner devices, in which the resistance at low $T$ is comparable to the resistance at room $T$, Figure 2. Therefore, the small values of $\Delta R_{SV}/R_{sat}$ cannot be explained just by the high $R_{sat}$ at low temperatures.

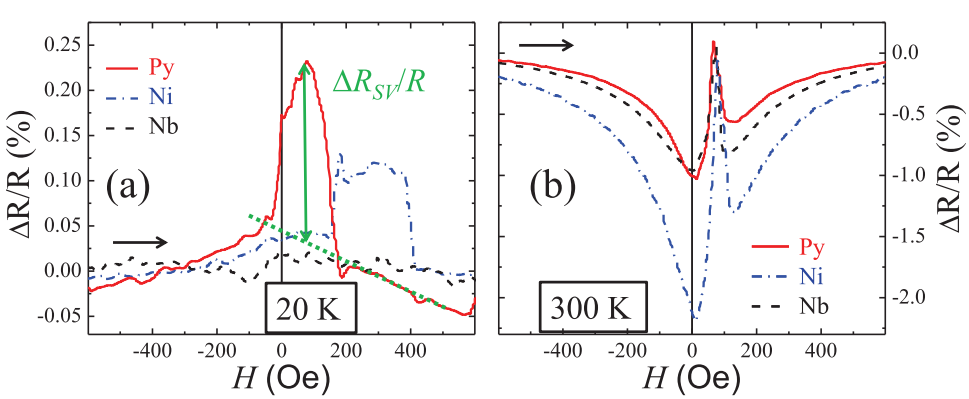


FIG. 5. Magnetoresistance measurements (a) at 20 K and (b) at 300 K for three different samples (positive field sweep only—indicated by black arrows). Red solid line corresponds to a regular sample with Py as the top ferromagnetic layer, blue dotted-dashed line correspond to a sample with top Ni layer, black dashed line—top Nb layer. Thickness of $V_2O_3$ layer is 44 nm in samples with Py and Nb, and 65 nm in sample with Ni. Green dotted and arrow lines show how the $\Delta R_{SV}$ is extracted from the graph for the sample with Py.

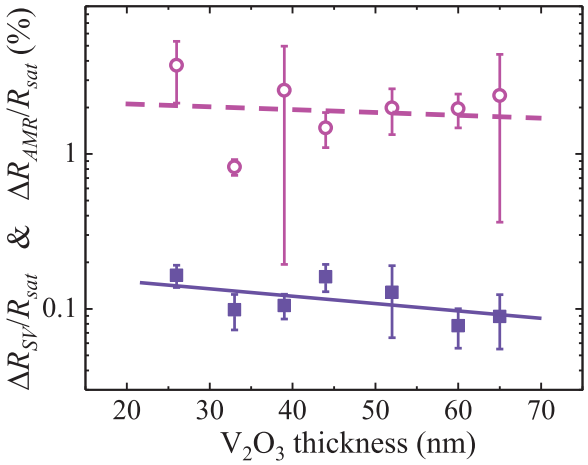


FIG. 6. $\Delta R_{SV}/R_{sat}$ and $\Delta R_{AMR}/R_{sat}$ as a function of $V_2O_3$ thickness. Solid blue squares correspond to the spin-valve effect at 20 K, empty magenta circles correspond to AMR effect at 300 K. The error bars indicate the standard deviation of the magnetoresistance measured for different devices with the same $V_2O_3$ thickness. Straight lines are guides to the eye, highlighting the difference between low and high temperature MR.

We used a two-channel model[29,35,36] to calculate the expected size of the spin-valve effect by two different methods. First, we used the equivalent resistance model[27,29,37,38] which is valid if the spin diffusion length (distance traveled by an electron before it loses its spin information) of $V_2O_3$ is assumed to be much larger than its thickness. In this approach, the total resistance is calculated as two parallel resistances, one for spin-up and another for spin-down channels, Figure 7(a). The resistance of each channel is a sum of corresponding resistances of two FM and one NM layers. If we assume that both FM layers are identical for simplicity, then for P configuration the resistances of the spin-up and spin-down channels are

$$2R_{F\uparrow} + R'_N \quad \text{and} \quad 2R_{F\downarrow} + R'_N, \tag{1}$$

correspondingly, where NM resistance for each spin channel $R'_N = 2R_N$, twice the total CPP resistance of NM layer. The difference between channels is due to ferromagnetic materials, since they have different resistances for spin-up and spin-down electrons, $R_{F\uparrow} \neq R_{F\downarrow}$. For AP configuration, the resistance of both channels in this case is the same

$$R_{F\uparrow} + R_{F\downarrow} + R'_N. \tag{2}$$

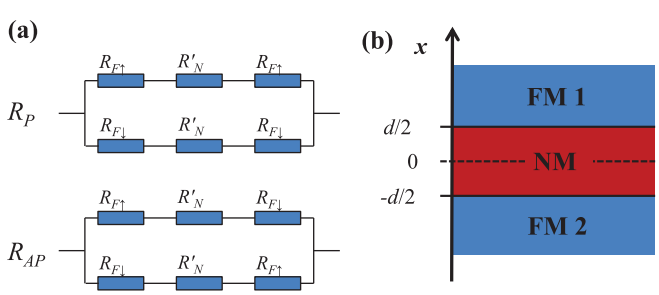


FIG. 7. (a) Equivalent resistance model of the FM/NM/FM device for P and AP states. (b) Schematics of a FM/NM/FM device with $x$-axis perpendicular to the layers.

The normalized magnetoresistance of the device is the difference between resistances for AP and P states, normalized to the resistance of the P state—the saturation resistance. After simplification, the result formula is the following:

$$\frac{\Delta R}{R_{sat}} = \frac{\alpha^2}{\left(\frac{R_N(1-\alpha^2)}{2R_F} + 1\right)^2 - \alpha^2}, \tag{3}$$

where $R_N$ and $R_F$ are the CPP resistances of FM and NM layers, and $\alpha$ is the FM polarization. Using measured CPP resistances of $V_2O_3$, 0.1–1 Ω, and calculated CPP resistance of FM layers is $\sim 3\,\mu\Omega$, and assuming that the average polarizations between Ni and Py is approximately $\sim 0.5$,[39–41] we roughly estimated $\Delta R/R_{sat}$, to be $\sim 10^{-11}$–$10^{-9}$. This is much smaller than the observed value of $10^{-3}$.

For the second approach, we assumed that the spin diffusion length of $V_2O_3$ is comparable to its thickness. In this approach, we take into account spin diffusion inside $V_2O_3$ and spin accumulation near the FM/$V_2O_3$ interfaces, which creates an additional voltage between the FMs.[35,36,38] For each of the regions, FM1, NM, and FM2 in Figure 7(b), chemical potential of each spin channel, $\mu_\uparrow$ and $\mu_\downarrow$, has the following general dependence on coordinate $x$:[38]

$$\begin{aligned} \mu_\uparrow &= A + Bx + \frac{C}{\sigma_\uparrow}\exp\left(-\frac{x}{\lambda}\right) + \frac{D}{\sigma_\uparrow}\exp\left(\frac{x}{\lambda}\right), \\ \mu_\downarrow &= A + Bx - \frac{C}{\sigma_\downarrow}\exp\left(-\frac{x}{\lambda}\right) - \frac{D}{\sigma_\downarrow}\exp\left(\frac{x}{\lambda}\right), \end{aligned} \tag{4}$$

where $\sigma_{\uparrow,\downarrow}$ are the conductivities of each spin channel, and $\lambda$ is the spin diffusion length. Equations provided by combination of boundary conditions at infinity and continuity of chemical potentials and currents at both FM/NM interfaces can be solved for $A$, $B$, $C$, and $D$ in each of the FM and NM regions. The solution allows calculation of additional voltage at the FM/NM interfaces due to the spin accumulation, which is different for P and AP states of the two FM layers.[42] The difference, normalized by the current, for our devices is estimated to be in $10^{-12}$ Ω range. However, in Figure 4(b), the measured signal is approximately 5 mΩ.

Thus, in both models, the predicted magnitude of the SV effect is much smaller than the magnitude measured in our devices. The reason for the small predicted values is usually assumed to originate from the so called resistivity mismatch[7,8]—a large resistivity difference between metallic FM and semiconducting NM materials produces an inefficient spin injection. In our devices at 20 K, the resistivity of Ni is $\sim 2.2\,\mu\Omega$ cm, whereas the resistivity of insulating $V_2O_3$ in Sec. IV was estimated to be in the Ω cm range. Because of the high resistivity of a semiconductor, there is a very limited number of carriers that can be injected into it, compared to the number of carriers a metal can deliver to the junction. Thus, almost equal numbers of the two spin types are injected resulting in zero net current polarization.[7] This can also be readily seen using the equivalent resistance model: if $R_N \gg R_F$, then the resistance of both channels becomes the same, see formula (3).

Tunnel barriers or highly resistive interfaces limit conduction into the semiconductor and help remedy this problem.[7,8,10,11] Thus, a possible explanation of a higher than expected spin-valve effect may reside in the formation of high resistance additional thin layers at the $V_2O_3$/Py and $V_2O_3$/Ni interfaces. However, this does not explain why the spin-valve effect is observed only below the transition. Since the resistance of the $V_2O_3$ decreases and the resistance of FM metal increases at higher T, then the efficiency of spin injection and, as a consequence, SV effect should increase. Moreover, $V_2O_3$ is reported to be antiferromagnetic at the temperatures below the transition. This long range spin ordering could create an additional polarization of the current inside $V_2O_3$, however, the exact mechanism is unclear.

Finally, another possible explanation could arise from the presence of pinholes and nano-shorts in the $V_2O_3$ layer. In the insulating state, the observed MR could be explained either by spin-tunneling through pinholes or by a SV effect in nano-shorts. In the metallic state, the effect would disappear because of the different current distribution and lower resistance of $V_2O_3$ layer. Contribution of the pinholes to the total resistance was estimated based on the analysis adopted from Ref. 43. The $V_2O_3$ thickness was assumed to have a Gaussian distribution around the nominal value, with the standard deviation equal to the roughness of the $V_2O_3$ film. Areas with zero or negative thickness were considered as shorts. Contribution of the shorts to the total measured resistance was found to increase exponentially with decreasing the $V_2O_3$ thickness. The tunneling MR and the SV effect are directly proportional to this contribution. Therefore, the observed MR below the transition temperature should significantly increase for lower thickness. Figure 6 indicates that this is not the case; therefore, the explanation due to the presence of pinholes is an unlikely one. Additional argument against this explanation is provided by the low temperature dependence of the measured resistance. Some of the devices exhibit metallic behavior below the transition temperature, while the others do not (see Figures 2 and 8(a)). Metallic behavior is explained by the presence of pinholes and nano-shorts. However, the SV effect is observed in both groups of the devices. Thus, it cannot be explained by the spin-tunneling through pinholes and SV effect in nano-shorts.

## IV. SIMULATION OF THE DEVICE

### A. Simulation details

To understand the details of the current and potential distributions and to estimate the resistivity of the $V_2O_3$ layer, we performed a quantitative analysis. More importantly, this analysis indicates the disappearance of the SV effect above the $V_2O_3$ transition temperature cannot be simply explained by the current redistribution in our devices.

We have used Comsol Multiphysics package to perform the 3-dimensional simulations of the device. Top view of the simulated structure is shown in Figure 1(c), which replicates a typical device with 10 $\mu$m-wide top and bottom electrodes with 90° corners. The length of each electrode was 20 $\mu$m. Cut corners (with 2 $\mu$m length of the diagonal line) and 0.5 $\mu$m mismatch between contacts were added to imitate

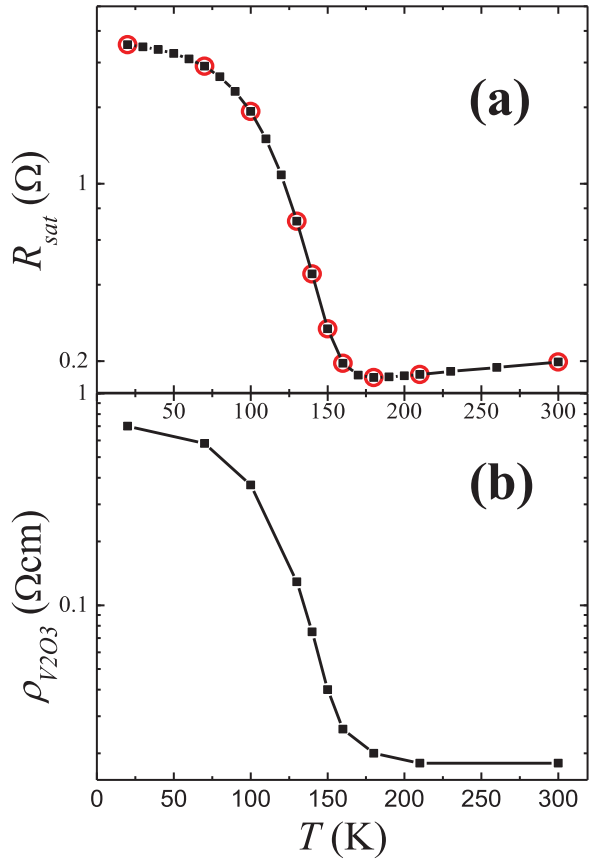


FIG. 8. (a) Example of a measured resistance as a function of temperature for a real device. (b) Resistivity of $V_2O_3$ obtained by matching the simulated and measured resistances for temperatures indicated by red circles on (a).

more closely the geometry of a typical experimental device shown in Figure 1(b). As a result, the electrodes form an intersection with cross sectional area equal to $(9.5 \times 9.5 - 2)$ $\mu m^2$, because of the misalignment and cut corners.

For simplicity, only 3 layers were included in the analysis – 40 nm bottom Ni contact, 44 nm $V_2O_3$ layer, and the top 200 nm gold contact. Other layers present in the real devices, such as 15 nm Py and 70 nm Cr layers, were not included because their sheet resistances were estimated to be 100–150 times (Py) and 15 times (Cr) larger than the sheet resistance of the top gold layer. Since these layers are in parallel with the gold layer along the whole top contact, then only a small portion of the current would flow in these layers.

The resistivity of Ni, $\rho_{Ni}$, and its temperature dependence were taken from the measurement of the bottom Ni contact in the real devices. The values used in the simulation varied between 2.2 $\mu\Omega$ cm at $T = 20$ K to 12 $\mu\Omega$ cm at 300 K. Because the resistivity of gold, $\rho_{Au}$, was not measured separately, the Comsol built-in values[44] were used for all temperatures.

A 1 mA current was applied to one side of the bottom Ni contact, marked with "$I+$" in Figure 1(c), while the opposite side of the top Au contact was set as ground, marked with "$I-$." Then the whole system was solved for voltage and current distributions. The resulting voltage difference was calculated between the ends of the bottom and the top contacts, not used for applying the current (marked with "$V+$" and

"$V-$" in Figure 1(c)). The simulated resistance, $R_{sim}$, was calculated by dividing the voltage difference by the applied current.

Figure 8(a) shows an example of temperature dependence of the resistance measured in a real device with $V_2O_3$ thickness of 44 nm. The measured resistance changes from approximately 3.5 Ω at 20 K to 0.2 Ω at 300 K. The resistivity of $V_2O_3$, $\rho_{V2O3}$, and its temperature dependence were not known. Therefore, we chose several characteristic temperatures, indicated by red circles, and simulated the device for various resistivities of $V_2O_3$ to match the simulated and measured values of the resistance. For each temperature, we used the appropriate $\rho_{Au}$ and $\rho_{Ni}$ values. Figure 8(b) shows the result of this matching where $\rho_{V2O3}$ changes from 0.7 Ω cm at 20 K to 0.018 Ω cm at 300 K with the transition around 150 K.

### B. Current distribution

Figures 9(a) and 9(b) show the distribution of the out-of-plane component of the current density inside the $V_2O_3$ layer. At 20 K, the current is distributed equally over the whole $V_2O_3$ layer at the junction (the part of $V_2O_3$ layer between the top and the bottom contacts). However, at 300 K, most of the current passes through $V_2O_3$ layer near the edge of the top Au contact. Moreover, independently of the current density at all temperatures, the direction of the current inside $V_2O_3$ varies between 87° and 90° from the plane of the sample.

### C. Contributions to the simulated resistance

Inhomogeneous current distribution in a device with large lateral dimensions may lead to artifacts. For example, the voltage might be measured in the part of the device where the current density is very small. This leads to a much smaller measured resistance than expected.[27] Although the quantitative analysis provides exact 3-dimensional potential distribution in our devices, it is still unclear how different materials contribute to the voltage measured between the side electrodes. Therefore, to estimate the relative contributions of Ni, Au, and $V_2O_3$ layers to the total simulated resistance, we took the following approach.

The simulated resistance is a function of all 3 materials resistivities $R_{sim} = f(\rho_{V2O3}, \rho_{Ni}, \rho_{Au})$. A first order Taylor expansion around $\rho'_{V2O3}, \rho'_{Ni}, \rho'_{Au}$ is given as

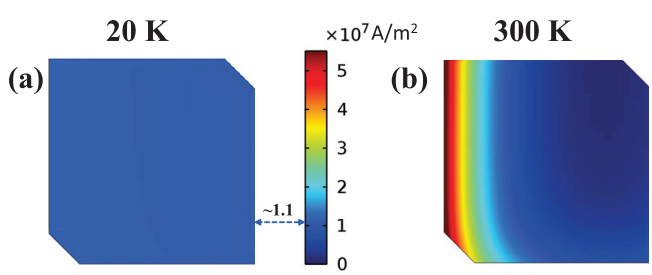


FIG. 9. (a) 20 K out-of-plane component of the current density across the $V_2O_3$ layer, corresponding to the area of the device marked by red dashed contour in Figure 1(c). (b) Same as (a) but at 300 K. Color-scale of the current density is the same for both (a) and (b).

$$\begin{aligned} R_{sim} = {} & f(\rho'_{V2O3}, \rho'_{Ni}, \rho'_{Au}) \\ & + \frac{\partial f(\rho'_{V2O3}, \rho'_{Ni}, \rho'_{Au})}{\partial \rho_{V2O3}} (\rho_{V2O3} - \rho'_{V2O3}) \\ & + \frac{\partial f(\rho'_{V2O3}, \rho'_{Ni}, \rho'_{Au})}{\partial \rho_{Ni}} (\rho_{Ni} - \rho'_{Ni}) \\ & + \frac{\partial f(\rho'_{V2O3}, \rho'_{Ni}, \rho'_{Au})}{\partial \rho_{Au}} (\rho_{Au} - \rho'_{Au}). \end{aligned} \tag{5}$$

Thus, we can write the simulated resistance as a linear function

$$R_{sim} = A\rho_{V2O3} + B\rho_{Ni} + C\rho_{Au} + D, \tag{6}$$

where $A$, $B$, and $C$ are the corresponding partial derivatives (for example, $A = \partial f(\rho'_{V2O3}, \rho'_{Ni}, \rho'_{Au})/\partial \rho_{V2O3}$), and $D$ is the sum of all constants in formula (5)

$$\begin{aligned} D = {} & f(\rho'_{V2O3}, \rho'_{Ni}, \rho'_{Au}) - \frac{\partial f(\rho'_{V2O3}, \rho'_{Ni}, \rho'_{Au})}{\partial \rho_{V2O3}} \rho'_{V2O3} \\ & - \frac{\partial f(\rho'_{V2O3}, \rho'_{Ni}, \rho'_{Au})}{\partial \rho_{Ni}} \rho'_{Ni} - \frac{\partial f(\rho'_{V2O3}, \rho'_{Ni}, \rho'_{Au})}{\partial \rho_{Au}} \rho'_{Au}. \end{aligned} \tag{7}$$

To estimate the individual contributions of the first 3 terms in Eq. (6), we vary each variable slightly and determine the change in the whole sum. For example, to find the relative contribution of the first term, $A\rho_{V2O3}/R_{sim}$, we increase the resistivity of $V_2O_3$ by $\Delta\rho_{V2O3}$, and calculate the change in $R_{sim}$. Since the simulated resistance increases by $\Delta R_{sim} = A\Delta\rho_{V2O3}$, then

$$\frac{\Delta R_{sim}}{R_{sim}} = \left(\frac{A\rho_{V2O3}}{R_{sim}}\right) \frac{\Delta\rho_{V2O3}}{\rho_{V2O3}}. \tag{8}$$

We performed this analysis for temperatures marked by red circles in Figure 8(a) using the $V_2O_3$ resistivity obtained from fitting the resistivity vs. $T$, Figure 8(b), and the corresponding Ni and Au resistivities. The results, shown in Figure 10, indicate that at low temperature most of the simulated resistance is due to the voltage drop across the $V_2O_3$ layer. However, at higher temperatures, the contribution of the bottom Ni layer raises up to approximately 40%, while the contribution of $V_2O_3$ layer drops below 60%. The high relative contribution of the Ni layer explains the observed AMR in this material at high $T$. The contribution of the top Au layer is much lower and reaches approximately 5% at 300 K.

### D. Observation of the SV effect

The analysis so far does not include the possible voltage drops across the FM/$V_2O_3$ interfaces due to the possible spin accumulation.[35] These voltage drops, if present, should be proportional to the current,[36,38] should have the same sign at both interfaces (for example, see Fig. 7 in Ref. 42), and should reverse sign for opposite current direction.[45] Therefore, the voltage drops due to the spin accumulation can be simulated

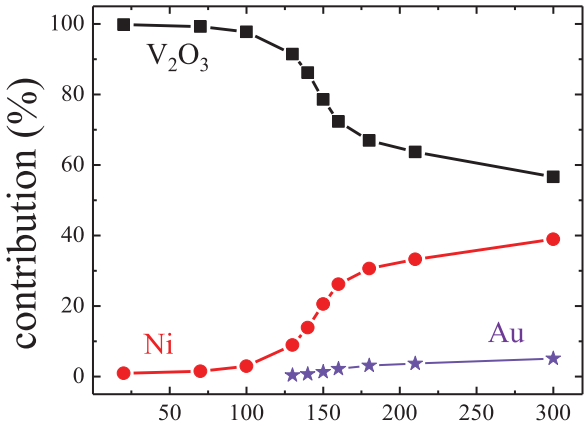


FIG. 10. Relative contributions of $V_2O_3$ (black squares), Ni (red circles), and Au (violet stars) as a function of temperature.

by additional layers, placed on both Ni/$V_2O_3$ and Au/$V_2O_3$ interfaces, with a thickness $th_i$ and anisotropic resistivity tensor. Resistivity of these interface layers (ILs) was set to be infinite for the in-plane directions (zero conductivity). This prohibits the current flow parallel to the Ni/$V_2O_3$ or $V_2O_3$/Au interfaces. The out-of-plane resistivity was calculated to be such that the out-of-plane resistance of each IL, $R_i$, was equal to approximately 0.1% of $R_{sim}$. Thus, these ILs provide additional voltage difference when current flows across Ni/$V_2O_3$ or $V_2O_3$/Au interfaces. We took 0.1% value because it is on the same order of magnitude as the SV effect measured in our devices at low temperatures. By turning the ILs on and off, we simulated the switching between AP and P states of FM layers, correspondingly. We calculated the change in the simulated resistance, $\Delta R = R_{sim}(with\ ILs) - R_{sim}(without\ ILs)$. The magnitude of $\Delta R/R_{sim}$ simulates the SV effect $\Delta R_{SV}/R_{sat}$, and indicated if the SV effect is measurable in the device or not, irrespective of the current distribution.

Figure 11 shows how the normalized difference in simulated resistance, $\Delta R/R_{sim}$, changes with temperature. Because of the uniform current distribution in $V_2O_3$ layer at low $T$, the difference corresponds to the sum of two additional interface resistances $R_i$ (since $R_i = 0.1\% \cdot R_{sim}$, the value $\Delta R/R_{sim} = 0.2\%$ is recovered). Above the transition temperature,

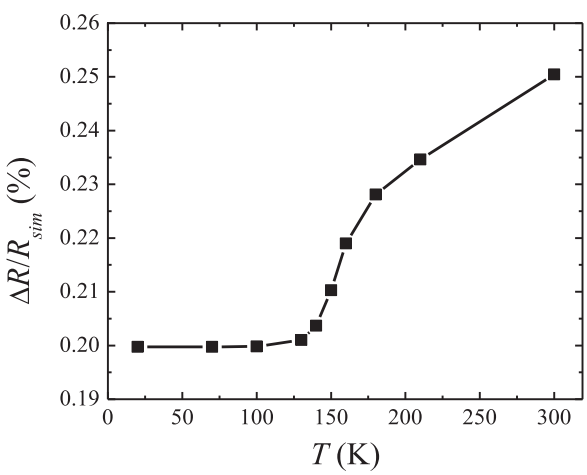


FIG. 11. Dependence of simulated $\Delta R/R_{sim}$ on temperature. This simulates the expected temperature dependence of $\Delta R_{SV}/R_{sat}$.

Figure 11 indicates that the inhomogeneous current distribution increases the simulated SV effect in our geometry: $\Delta R/R_{sim}$ reaches 0.25% at 300 K. Moreover, $\Delta R/R_{sim}$ does not decrease below 0.2% for any temperatures.

This result implies that if there is an additional voltage drop at the FM/$V_2O_3$ interfaces due to the possible spin accumulation then it should be measurable in our devices at all temperatures.

### E. Effect of misalignment

Finally, we investigated the effect of the misalignment between the top and the bottom contacts. We characterize the misalignment by the resulting overlap area between the top and the bottom contacts. *Negative* misalignments lead to smaller areas (example shown in Figure 1(c)), while *positive* misalignments lead to larger areas. We found that for negative misalignment the simulated resistance and the contributions of Ni and Au increase, while the contribution of $V_2O_3$ decreases. Conversely, for positive misalignment of the contacts the effect is reversed. The normalized difference in simulated resistance $\Delta R/R_{sim}$ was found to increase with negative misalignments, and decrease with positive. For example, at 300 K and negative misalignment by 0.5 $\mu$m, we showed that $\Delta R/R_{sim} = 0.25\%$, Figure 11; for the same temperature and zero misalignment, it is approximately 0.23%; and for positive 0.5 $\mu$m it is 0.19%. Thus, the misalignment may affect the amplitude of the measured SV signal, but it cannot eliminate it completely.

## V. SUMMARY

We have measured spin valve devices composed of Ni, $V_2O_3$, and Py layers in the CPP geometry. $V_2O_3$ grown on Ni in the (001) direction exhibits a metal insulator transition at ~160 K for all fabricated thicknesses from 13 nm to 65 nm. Magnetoresistances at temperatures above the MIT are solely due to the AMR of the bottom Ni contact. The normalized amplitude of the magnetoresistance at high T is approximately 1%–2% and is consistent with AMR reported in literature. At low temperatures, a ~0.1% spin-valve (SV) effect is observed. However, this is 6–9 orders of magnitude larger than theoretically predicted. The relatively large measured spin-valve effect may be due to a combination of high resistance $V_2O_3$/Ni and $V_2O_3$/Py interfaces, together with additional polarization produced by the low temperature antiferromagnetism of $V_2O_3$. Surprisingly, the spin valve effect disappears at the MIT, contrary to expectations based on the resistivity mismatch effect.

Finite element analysis of our devices showed that at low temperatures the current distribution is homogeneous across the devices cross-section, but at high temperatures the current is concentrated near the edge of the top Au contact. Moreover, the current flows perpendicular to the $V_2O_3$ layer even at 300 K. We simulated the relative contributions of the various constituents to the simulated resistance. At low temperature, the simulated resistance is principally (~100%) due to the voltage drop across the $V_2O_3$ layer. However, at higher temperatures, the contribution of the bottom Ni layer rises up to 40% while the contribution of $V_2O_3$ layer drops

below 60%, which explains the observed AMR of Ni at high $T$. The contribution of the top Au layer is smaller than 5% at all temperatures.

We simulated an additional voltage drop across the $FM/V_2O_3$ interfaces due to the possible spin accumulation by adding extra layers with anisotropic resistivity. The changes in the simulated resistance were observed on the same order of magnitude for all values of material resistivities. This indicates that the absence of SV effect above MIT cannot be explained by changes in the current distribution in the device.

## ACKNOWLEDGMENTS

We thank Thomas Saerbeck for useful comments and careful reading of the manuscript, and Ilya Valmianski for estimating the dependence of pinholes resistance on thickness. The magnetism aspects of this work were supported by the Office of Basic Energy Sciences, U.S. Department of Energy, under Grant No. DE FG03-87ER-45332 and the oxide related science by the AFOSR Grant No. FA9550-12-1-0381.

[1]I. Zutic, J. Fabian, and S. Das Sarma, Rev. Mod. Phys. **76**, 323 (2004).
[2]J. Sinova and I. Zutic, Nature Mater. **11**, 368 (2012).
[3]S. Maekawa, T. Tohyama, S. E. Barnes, S. Ishihara, W. Koshibae, and G. Khaliullin, *Physics of Transition Metal Oxides* (Springer-Verlag, Berlin, Heidelberg, 2004).
[4]C. N. R. Rao, Annu. Rev. Phys. Chem. **40**, 291 (1989).
[5]M. Bibes and A. Barthelemy, IEEE Trans. Electron Devices **54**, 1003 (2007).
[6]J. Nogues and I. K. Schuller, J. Magn. Magn. Mater. **192**, 203 (1999).
[7]G. Schmidt, D. Ferrand, L. W. Molenkamp, A. T. Filip, and B. J. van Wees, Phys. Rev. B **62**, R4790 (2000).
[8]B. Jonker, *Handbook of Spin Transport and Magnetism* (Chapman and Hall/CRC, Boca Raton, FL, 2011), p. 329.
[9]R. Jansen, Nature Mater. **11**, 400 (2012).
[10]R. Godfrey and M. Johnson, Phys. Rev. Lett. **96**, 136601 (2006).
[11]E. I. Rashba, Phys. Rev. B **62**, R16267 (2000).
[12]M. Imada, A. Fujimori, and Y. Tokura, Rev. Mod. Phys. **70**, 1039 (1998).
[13]F. J. Morin, Phys. Rev. Lett. **3**, 34 (1959).
[14]D. Adler, Rev. Mod. Phys. **40**, 714 (1968).
[15]J. de la Venta, M. Erekhinsky, S. Wang, K. West, R. Morales, and I. Schuller, Phys. Rev. B **85**, 134447 (2012).
[16]Overall, more than 20 samples were fabricated with 6 devices on each sample, but due to complications during the fabrication process the magnetoresistance of only about 50 devices are presented in this study.
[17]W. P. Pratt, Jr., S. F. Lee, J. M. Slaughter, R. Loloee, P. A. Schroeder, and J. Bass, Phys. Rev. Lett. **66**, 3060 (1991).
[18]We have also cooled some of the samples to 10 K in various applied magnetic fields; however, this does not change the magnetoresistance measurements, implying the absence of exchange bias in the system.
[19]B. Sass, C. Tusche, W. Felsch, N. Quaas, A. Weismann, and M. Wenderoth, J. Phys.: Condens. Matter **16**, 77 (2004).
[20]B. S. Allimi, S. P. Alpay, C. K. Xie, B. O. Wells, J. I. Budnick, and D. M. Pease, Appl. Phys. Lett. **92**, 202105 (2008).
[21]S. Yonezawa, Y. Muraoka, Y. Ueda, and Z. Hiroi, Solid State Commun. **129**, 245 (2004).
[22]J. Brockman, N. P. Aetukuri, T. Topuria, M. G. Samant, K. P. Roche, and S. S. P. Parkin, Appl. Phys. Lett. **98**, 152105 (2011).
[23]C. Grygiel, C. Simon, B. Mercey, W. Prellier, R. Fresard, and P. Limelette, Appl. Phys. Lett. **91**, 262103 (2007).
[24]D. A. Rabson, B. J. Jonsson-Akerman, A. H. Romero, R. Escudero, C. Leighton, S. Kim, and I. K. Schuller, J. Appl. Phys. **89**, 2786 (2001).
[25]T. McGuire and R. Potter, IEEE Trans. Magn. **11**, 1018 (1975).
[26]W. Thomson, Proc. R. Soc. London **8**, 546 (1856).
[27]M. A. M. Gijs and G. E. W. Bauer, Adv. Phys. **46**, 285 (1997).
[28]B. Jack, *Handbook of Spin Transport and Magnetism* (Chapman and Hall/CRC, Boca Raton, FL, 2011), p. 69.
[29]E. Tsymbal, D. Pettifor, and S. Maekawa, *Handbook of Spin Transport and Magnetism* (Chapman and Hall/CRC, Boca Raton, FL, 2011), p. 95.
[30]M. N. Baibich, J. M. Broto, A. Fert, F. N. Van Dau, F. Petroff, P. Etienne, G. Creuzet, A. Friederich, and J. Chazelas, Phys. Rev. Lett. **61**, 2472 (1988).
[31]G. Binasch, P. Grünberg, F. Saurenbach, and W. Zinn, Phys. Rev. B **39**, 4828 (1989).
[32]B. Dieny, V. S. Speriosu, S. S. P. Parkin, B. A. Gurney, D. R. Wilhoit, and D. Mauri, Phys. Rev. B **43**, 1297 (1991).
[33]M. Kovylina, M. Erekhinsky, R. Morales, J. Villegas, I. Schuller, A. Labarta, and X. Batlle, Appl. Phys. Lett. **95**, 152507 (2009).
[34]I. Rhee and K. Chan, IEEE Trans. Magn. **37**, 1032 (2001).
[35]P. C. van Son, H. van Kempen, and P. Wyder, Phys. Rev. Lett. **58**, 2271 (1987).
[36]T. Valet and A. Fert, Phys. Rev. B **48**, 7099 (1993).
[37]S. F. Lee, W. P. Pratt, Jr., R. Loloee, P. A. Schroeder, and J. Bass, Phys. Rev. B **46**, 548 (1992).
[38]F. Jedema, M. Nijboer, A. Filip, and B. van Wees, Phys. Rev. B **67**, 085319 (2003).
[39]M. Erekhinsky, A. Sharoni, F. Casanova, and I. Schuller, Appl. Phys. Lett. **96**, 022513 (2010).
[40]S. Dubois, L. Piraux, J. George, K. Ounadjela, J. Duvail, and A. Fert, Phys. Rev. B **60**, 477 (1999).
[41]P. Holody, W. Chiang, R. Loloee, J. Bass, W. Pratt, and P. Schroeder, Phys. Rev. B **58**, 12230 (1998).
[42]J. F. Gregg, I. Petej, E. Jouguelet, and C. Dennis, J. Phys. D: Appl. Phys. **35**, R121 (2002).
[43]C. Monton, I. Valmianski, and I. K. Schuller, Appl. Phys. Lett. **101**, 133304 (2012).
[44]R. A. Matula, J. Phys. Chem. Ref. Data **8**, 1147 (1979).
[45]F. Casanova, A. Sharoni, M. Erekhinsky, and I. Schuller, Phys. Rev. B **79**, 184415 (2009).